Electronic Supplementary Information (ESI) for "Visualizing Reaction and Diffusion in Xanthan Gum Aerosol Particles Exposed to Ozone"

Peter A. Alpert[*a], Pablo Corral Arroyo[a,b], Jing Dou[c], Ulrich K. Krieger[c], Sarah S. Steimer[d], Jan-David Förster[e], Florian Ditas[e], Christopher Pöhlker[e], Stéphanie Rossignol[f,g], Monica Passananti[f,h,i], Sebastien Perrier[f], Christian George[f], Manabu Shiraiwa[j], Thomas Berkemeier[k], Benjamin Watts[l] and Markus Ammann[*a]

[a]Laboratory of Environmental Chemistry, Paul Scherrer Institute, 5232 Villigen PSI, Switzerland

[b]Institute for Atmospheric and Climate Science, ETH Zürich, 8092 Zurich, Switzerland.

[c]Institute for Physical Chemistry, ETH Zürich, 8092 Zurich, Switzerland.

[d]Department of Chemistry, University of Cambridge, Cambridge, CB2 1EW, United Kingdom.

[e]Multiphase Chemistry Department, Max Planck Institute for Chemistry, 55128 Mainz, Germany.

[f]Univ. Lyon, Université Claude Bernard Lyon 1, CNRS, IRCELYON, F-69626, Villeurbanne, France

[g]Aix Marseille Université, CNRS, LCE UMR 7376, 13331 Marseille, France.

[h]Institute for Atmospheric and Earth System Research/Physics, Faculty of Science, University of Helsinki, 00710, Helsinki, Finland

[i]Dipartimento di Chimica, Università di Torino, Via Giuria 5, 10125 Torino, Italy

[j]Department of Chemistry, University of California, Irvine, CA 92617, United States

[k]School of Chemical & Biomolecular Engineering, Georgia Institute of Technology, Atlanta, GA 30332, United States

[l]Laboratory for Synchrotron Radiation-Condensed Matter, Paul Scherrer Institute, 5232 Villigen PSI, Switzerland

[*]Corresponding authors Peter.Alpert@psi.ch and Markus.Ammann@psi.ch

1 Detailed Methods

1.1 Particle preparation

Particles were generated from an ultrasonic nebulizer[1] containing a dilute aqueous solution of xanthan gum (XG) and $FeCl_2$ at concentrations of 0.1 mM and 1.0 mM, respectively, in ultrapure water (18 MΩ cm, MilliQ). XG dissolves easily leading to a pH of ~ 5 in aqueous solution[2]. Mixed XG/$FeCl_2$ particles were carried in N_2 gas through a Nafion membrane diffusion drier, bipolar Kr-85 neutralizer and a custom built differential mobility analyzer (DMA) to select a dry mobility diameter of ~ 280 nm. The relative humidity, RH, inside the DMA was about $25 \pm 5\%$. Mobility selected particles were impacted onto flat silicon nitride membranes with an aerosol flow of 0.7 L min^{-1}. Fe^{2+} in particles exposed to ambient air completely oxidized within 1 day sitting open to the laboratory. To avoid this, particles were placed in a dry, dark and evacuated box immediately after impaction for storage and transport to the experimental station. The time between solution preparation, aerosol generation, impaction and storage was ~ 30 min. Storage time under vacuum was between 30 min to 12 hour in addition. This ensured a high initial Fe^{2+} concentration.

1.2 Microreactors

Helium was used as a carrier gas for both the PolLux environmental microreactor[3] and the MPI-C aerosol micro-reactor[4]. A fraction of the total dry He flow was diverted to a humidifier consisting of a temperature controlled chamber half filled with water. Nafion$^{\text{TM}}$ film separated the water and humidified He flow that exited the humidifier and mixed with the remaining dry flow. Dry and humidified He flow rates were adjusted depending on the desired RH. The RH and temperature, T, of the gas was measured with two calibrated sensors up and down stream of the microreators to calculate the water partial pressure in the gas entering a microreactor. The cell temperature of 20° C was assumed equal to the particle temperature, T_p, and was kept constant using a continual cooling source and a controlled counter-heater. We performed regular checks of the deliquescence relative humidity of NaCl yielding an accuracy of $\pm 2\%$ in RH. The gas phase ozone concentration, $[O_3]_\text{g}$, was measured at the outlet of each cell using a UV-absorption setup, which was calibrated against a commercial ozone monitor (Teledyne

51 Mo. T400) at $T = 20\ °C$ and ambient pressure of 975 mbar with an accuracy $< \pm0.5\%$.

52 The procedure for our experiments is as follows. Particles were generated, dried, impacted onto silicon

53 nitride substrates and mounted in one of the two microreactors. Particle diameters on all samples were

54 between 0.2 and 4.0 μm. Then, the microreactor was mounted in the vacuum chamber for analysis

55 with scanning transmission X-ray microscopy coupled with near-edge X-ray absorption fine structure

56 spectroscopy (STXM/NEXAFS) described later. Using STXM/NEXAFS, the Fe^{2+} fraction, α, was

57 determined in vacuum, then at a pressure of 150 or 450 mbar under He only for the PolLux environmental

58 microreactor and the MPI-C aerosol micro-reactor, respectively, and at pressure under He and exposed

59 to O_2 and humidity. After O_2 exposure was completed, the UV lamp was switched on without any

60 change to the sample flow. This resulted in increasing $[O_3]_g$ in the microreactor as a function of t shown

61 in Fig. S1. During O_2 and O_3 exposure, Fe oxidation state was continuously measured as described

62 in the next sections. This procedure was applied to experiments where $RH = 0$, 40 and 80%. At the

63 end of the experiment at $RH = 0\%$, the ozone lamp was switched off allowing for sufficient time (~ 10

64 min) to reduce $[O_3]_g$ to background levels. Then, RH was increased to 20% without any change to

65 the O_2 flow and Fe oxidation state was continuously monitored over hours. Afterward, the UV lamp

66 was switched on again to exposure the particles to O_3 at $RH = 20\%$. This procedure was repeated for

67 $RH = 60\%$, thus the data for O_2 and O_3 exposure at $RH = 0$, 20 and 60% was obtained from a single

68 sample in succession. Experiments where $RH = 40$ and 80% employed different samples generated from

69 independently prepared solutions.

1.3 STXM/NEXAFS analysis

71 Transmitted photons were measured to determine optical density, OD, using STXM/NEXAFS. Images

72 of the same particles were obtained at discrete X-ray energy steps and digitally aligned[5]. Hundreds of

73 images acquired at small steps of about 0.1 or 0.2 eV are referred to as a "stack" of images. Averaging

74 the OD over each pixel in an aligned stack that made up imaged particles as a function of X-ray energy

75 yielded a NEXAFS spectrum. We note that acquiring a full stack (~ 100 images) to generate a NEXAFS

76 spectrum typically took about 30 min. A second method to generate a NEXAFS spectrum was to scan

77 a single line, referred to as a "line scan", as opposed to imaging a field of view (FOV) for a stack.

We investigated two X-ray energy ranges, 278-320 eV and 700-735 eV, which are the C K-edge and Fe L-edge absorption, respectively, and used stacks and linescans to generate full NEXAFS spectra seen in Fig. 1 of the main text and in Fig. S2a. At the C K-edge, absorption peaks were identified in the spectra that correspond to various bonding and oxygenated functionalities[6]. At the Fe L-edge, two absorption peaks over an X-ray energy range of roughly $705 - 713$ and $718 - 727$ eV corresponding to L_3 $2p_{3/2}$ and L_2 $2p_{1/2}$ orbitals, respectively, were identified. The former has exceptional absorption and typically exhibits an OD about 10 times that of the edge step, which we use to calculate the Fe oxidation state as either ferrous (Fe^{2+}) or ferric (Fe^{3+}) with their peaks at X-ray energies of 707.9 and 709.6 eV. Generally speaking, this dipole transition to 3d states has a large Coulomb interaction and thus is highly dependent on the local electronic structure. Resolving power used here was $\Delta E/E = 0.0018$. This meant that we were capable of resolving peaks separated by 1.3 eV at the Fe L-edge. Ferrous and ferric iron peaks are separated by about 1.7 eV and thus, easily distinguished. When associated with other organic species or water, the chemical environment surrounding Fe atoms may slightly alter the energy positions of these peaks[7,8]. We note that it was impossible to generate particles on substrates with a pure Fe^{2+} content. As previously discussed, particles were exposed to laboratory air when moved from the nebulizer to a sealed vacuum container for transport to the PolLux beamline and again when mounting the particle samples to the microreactors. A small, but non-negligible amount of oxidation took place. The presence of Fe^{2+} and small amounts of Fe^{3+} was in turn, an advantage and used to identify peak X-ray absorption energies for Fe^{2+} and Fe^{3+} prior to any O_3 exposure.

1.4 Quantifying Fe^{2+} fraction, α

The high contrast between the main absorption features of Fe^{2+} and Fe^{3+} allowed quantification of the oxidation state of iron in aerosol particles. Moffet et al.[8] proposed a parameterization to quantify Fe^{2+} and Fe^{3+} in ambient iron and organic containing particles following

$$\alpha = \frac{[\text{Fe}^{2+}]}{[\text{Fe}_{\text{tot}}]} = \frac{c - dr}{c - a + br - dr}, \tag{S1}$$

where $a = 9.53548 \times 10^{-3}$, $b = 3.02169 \times 10^{-3}$, $c = 3.49723 \times 10^{-3}$ and $d = 9.94950 \times 10^{-3}$ are constants. r is the background subtracted peak height OD ratio,

$$r = \frac{OD_{\text{Fe}^{2+}} - OD_{\text{pre}}}{OD_{\text{Fe}^{3+}} - OD_{\text{pre}}}, \tag{S2}$$

where $OD_{\text{Fe}^{2+}}$ is the peak height for Fe^{2+}, $OD_{\text{Fe}^{3+}}$ is the peak height for Fe^{3+} and OD_{pre} is the optical density at the Fe pre-edge at X-ray energy between $\sim 690 - 703$ eV. Using stacks to determine OD_{pre}, $OD_{\text{Fe}^{2+}}$ and $OD_{\text{Fe}^{3+}}$ in eqn (S2) during oxidation would result in poor time resolution during O_3 exposure. Although a line scan took much less time (on the order of minutes) it could not provide a 2-D image of particles and thus lacked spatial information. Therefore, it was necessary to perform a third type of scan referred to here as a "map", which used only a few OD images at the most important X-ray energies (see Figs. S2a and b). This was advantageous because with a high 2-D spatial resolution, each pixel was exposed to X-rays only a few times, thus limiting the dose. Taking maps at peak absorption energies still allowed for observation of OD_{pre}, $OD_{\text{Fe}^{2+}}$ and $OD_{\text{Fe}^{3+}}$ used in eqn (S2) as only peak heights were required.

The time to acquire 4 OD images per map as done in Figs. S2b and S2c was ~ 10 min. In order to shorten this time by half (and thus double the number of particles analyzed), only two X-ray images per map were acquired during O_3 exposure at observed Fe^{2+} and Fe^{3+} peaks to derive $OD_{\text{Fe}^{2+}}$ and $OD_{\text{Fe}^{3+}}$. The following linear relationship seen in Fig. S3 for 226 particles was derived as

$$OD_{\text{pre}} = m(\overline{OD}_{\text{Fe}^{2+}} + \overline{OD}_{\text{Fe}^{3+}}), \tag{S3}$$

where $m = 0.178 \pm 0.002$ is the fitted slope parameter and standard error, $R^2 = 0.98$ and the root mean square error $\sigma_{\text{rms},OD_{\text{pre}}} = \pm 0.01$. $\overline{OD}_{\text{Fe}^{2+}}$, $\overline{OD}_{\text{Fe}^{3+}}$ and $\overline{OD}_{\text{pre}}$ were averaged over all pixels in a single particle. We then define the ratio,

$$r_{\text{raw}} = \frac{\overline{OD}_{\text{Fe}^{2+}}}{\overline{OD}_{\text{Fe}^{3+}}}, \tag{S4}$$

and substitute into eqn (S2) to yield the following equation,

$$r = \frac{r_{\text{raw}} - m(r_{\text{raw}} + 1)}{1 - m(r_{\text{raw}} + 1)}. \tag{S5}$$

5

Finally, r from eqn (S5) is substituted into eqn (S1) to obtain an average value of α. Uncertainty in α has been calculated as the error on the average and propagated through quadrature. We acknowledge that in addition to random error, some systematic error can exist due to e.g. microscope alignment, minor instrument vibrations and extraneous noise in the electron beam used to generate X-rays. The use of thousands of particles, each having hundreds or thousands of pixels, was more than sufficient to evaluate the random error by observing the scatter in the data, which was about ± 0.07. Error in α was determined to be either the propagated error or ± 0.07, whichever was larger.

1.5   Assessment of X-ray beam damage

In all experiments, we determined X-ray exposure for observing r as to not damage the particles. When X-rays irradiated particles which already experienced oxidation, photochemical reaction with X-ray light reduced Fe^{3+} back to Fe^{2+}. This was a potential bias in observed OD which would lead to α higher than actual values. To quantify this bias, we repeated scans (stacks and linescans) on particles and observed changes in the NEXAFS spectra. We found that it was impossible to avoid X-ray induced Fe reduction (as seen in Fig. S2a) and simultaneously acquire NEXAFS spectra with sufficient signal. Therefore, stacks and linescans could not be used to quantify α, however, they could be used to obtain the X-ray energy at peak OD. In no instance did we observe X-ray damage which oxidized Fe^{2+} to Fe^{3+} even in the presence of O_2 or O_3.

X-ray exposure is defined here as the incident photon count, I_0, over a pixel, which was controlled by adjusting the time that the X-ray beam remained over a single pixel and the X-ray intensity. We took 4 consecutive maps, each having 4 energy points over the same FOV and observed $OD_{Fe^{2+}}$ and $OD_{Fe^{3+}}$ seen in Fig. S2b, where $I_0 = 250$ counts per pixel approximately for each energy. No change in OD was observed as seen in Fig. S2b. Therefore, beam damage could be avoided up to $I_0 = 1000$ counts per pixel, which was used to quantify α without bias using maps. When $I_0 = 800$ counts per pixel, we did observe changes in $OD_{Fe^{2+}}$ and $OD_{Fe^{3+}}$ after irradiating twice as seen in Fig. S2c. This implies that X-ray irradiation at $I_0 = 1000$ counts per pixel for 4-energy maps was close to optimal to simultaneously minimize X-ray beam damage and measure the greatest absorption signal. As previously mentioned, we derived α using 2-energy maps as opposed to 4-energy maps used for testing beam damage, and thus

6

are certain to have avoided it when acquiring data.

1.6 Particle exposure to O_2 and O_3

Particles were exposed to O_2 prior to O_3 for all experiments. Figure S4 shows the change in α over O_2 exposure time where each data point was determined from an average of about 5-25 particles in a single image. The error bars on each point demonstrate the propagated error, which is typically smaller than ± 0.07 as previously mentioned. Figure S5 shows α for each particle irrespective of time as a function of circle equivalent particle diameter, d_{p}. Error bars are the propagated error and appear much smaller than the data scatter. The standard deviation of α in Fig. S5 was determined and plotted as dashed lines in Fig. S4. Calculated α values all fell within this uncertainty range, which led us to place a conservative limit on our uncertainty of ± 0.07. After O_2 exposure experiments were finished, the UV lamp was switched on causing an increase in O_3 concentration over time as seen in Fig. S1. This error derived for O_2 exposure was also applied to O_3 exposure experiments.

## 1.7 Modeled 3-D radial profiles and column integrated 2-D profiles

The 2-D column integrated values of α were determined from STXM/NEXAFS, however it was necessary to compare with those derived from the KM-SUB model. This was accomplished by first determining the volume of every modeled spherical shell projected onto a 2-D grid point with the same resolution as the images acquired from STXM/NEXAFS. Each shell over a grid box (pixel) contributes a fraction of the total volume extending from the silicon nitride surface to the top of the particle. Therefore, α for a single grid point is calculated as the volume weighted average of each shell piece within a grid point. Figure S6 shows a graphical representation of a modeled spherical particle and a projected volume of a shell onto a pixel in the $x - y$ plane. The KM-SUB model predicted 3-D radial concentrations in spherical shells having variable thickness. An arbitrary pixel having one corner at coordinates (x, y) has the opposite corner at $(x + \Delta x), (y + \Delta y)$, where $\Delta x = \Delta y = 35$ nm is the spatial resolution from STXM/NEXAFS. For all shells, we integrated the sphere equation in Cartesian coordinates over all pixels from $r = 0 \rightarrow r_i$, where r_i is the outside diameter of ith shell. For a single pixel, we subtracted the difference in adjacent spherical volumes to derive the projected spherical shell volume. Finally, we

computed a volume weighted average in α in a single pixel over all shells. A pixel at the center of a modeled particle with $d_{\mathrm{p}} = 0.5$ μm, would have the contribution of α values from all modeled shells. However, a pixel extending 35 nm from the particle perimeter, would only have a volume contribution from modeled layers extending 35 nm from the particle surface. The 2-D projected α calculated for pixels extending from the center to the perimeter was then directly compared with observations.

Model predicted 3-D profiles in α were much sharper than those in 2-D. At $RH = 60\%$ for example, α dropped by ~ 0.5 over a 500 nm particle radius in 3-D after 1 hr of reaction. The conversion to 2-D profiles yielded a drop in α by ~ 0.2 for the same length scale. Despite the integration described above, 2-D profiles remain highly sensitive to changes in 3-D as seen in Fig. S7. Hypothetically speaking, depletion over t from $\alpha = 0.9$ to 0.5 (Fig. S7a) could potentially look completely uniform throughout the entire volume (Fig. S7c) or completely inhomogeneous with 2 spherical shell regions, e.g. having $\alpha = 0$ in the outer shell and 0.9 in the inner shell (Fig. S7b). These two cases would result in a homogeneous or a sharply increasing 2-D α profile (Fig. S7d). This degree of homo- or inhomogeneity was never observed, and instead was always in between these extremes. We note that a spatial inversion of our data was not performed, i.e. from observed 2-D column integrated profiles to 3-D radial profiles. This would require data smoothing, constrained values or use of assumed functional forms because error and data scatter in inverting 2-D to 3-D profiles would propagate cumulatively from the exterior to the interior of particles potentially growing to infinity.

1.8   Parameters used in the KM-SUB model

We used a net bulk reaction

$$2\,\mathrm{Fe}^{2+} + \mathrm{O}_3 \xrightarrow{2H+} 2\,\mathrm{Fe}^{3+} + \mathrm{O}_2 + \mathrm{H}_2\mathrm{O}, \tag{R3}$$
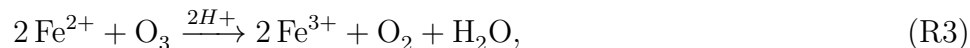
where $k_{R3} = 3.7 \times 10^5$ M^{-1} s^{-1} or 6.2×10^{-16} cm^3 s^{-1} to model bulk O_3 reaction in our particles. The surface reaction rate coefficient, k_{slr1}, was assumed to be proportional to k_{R3} on a natural logarithmic scale with a proportionality constant derived from the ratio between bulk and surface reaction of O_3 with shikimic acid[1]. We set $k_{\mathrm{slr1}} = \exp\left(\delta_{\mathrm{sh}} \ln k_{R3}\right) = 6.3 \times 10^{-14}$ cm^2 s^{-1}, where $\delta_{\mathrm{sh}} = 0.868$ is the ratio between the surface and bulk reaction rate of shikimic acid with O_3 on a natural log scale. Parameters for O_3 utilized in KM-SUB are taken from previous work[9] and include the surface self reaction rate

constant, k_{slr2} [cm^2 s^{-1}], the surface accommodation coefficient, $\alpha_{s,0}$, the desorption lifetime, τ_{d,O_3} [s], the adsorption cross section for O$_3$, σ_{O_3} [cm^2], and the gas phase diffusion coefficient, $D_{g,O3}$ [cm^2 s^{-1}], at 150 mbar. The surface area occupied by an adsorbed Fe ion was $\sigma_{Fe} = 2 \times 10^{-16}$ cm^2, and was equivalent to the surface area of a sphere of the size of the Fe^{2+} ion in solution[10]. Parameters that depend on RH include the bulk to surface transfer rate coefficient, k_{bs,O_3}, the surface to bulk transfer rate coefficient, $k_{sb,Fe}$, and the equilibrium surface to bulk concentration ratio, K_{bs}, were determined from the following parameterizations fitted to previous values[9], where

$$k_{bs,O_3}[\text{cm s}^{-1}] = 0.6904 + 1.1675 e^{35.6235\left(\frac{RH}{100} - 0.8369\right)}, \tag{S6}$$

$$\ln k_{sb,Fe}[\text{s}^{-1}] = -9.2911 + 7.0439\frac{RH}{100} - 5.4626\left(\frac{RH}{100}\right)^2 - e^{30.7316\left(\frac{RH}{100} - 0.8484\right)}, \tag{S7}$$

and

$$\ln K_{bs}[\text{cm}] = -19.8434 - 1.5613\frac{RH}{100} + 3.1616\left(\frac{RH}{100}\right)^2, \tag{S8}$$

which are shown in Fig. S8. Parameter units above are given in brackets. Water uptake of XG as a function of RH has been previously quantified using a hygroscopicity factor, $\kappa = 0.08$[11]. We calculated the water concentration in particles assuming only XG contributes to water uptake and neglected water uptake due to FeCl$_2$.

2 Detailed Results and Discussion

2.1 Parameterization of diffusion coefficients and Henry's Law constants.

We use a Vignes type equation to derive an expression for the fitting parameters continuous in RH following

$$\log D_{O_3} = (x_w \alpha_{x_w}) \log D_{O_3}^\circ + (1 - x_w \alpha_{x_w}) \log D_{O_3}(RH = 0\%), \tag{S9}$$

$$\log D_{Fe} = (x_w \alpha_{x_w}) \log D_{Fe}^\circ + (1 - x_w \alpha_{x_w}) \log D_{Fe}(RH = 0\%), \tag{S10}$$

$$\log H_{O_3} = (x_w \alpha_{x_w}) \log H_{O_3}^\circ + (1 - x_w \alpha_{x_w}) \log H_{O_3}(RH = 0\%), \tag{S11}$$

and

$$\ln \alpha_{x_{\mathrm{w}}} = (1 - x_{\mathrm{w}})^2 [C + 3D - 4D(1 - x_{\mathrm{w}})], \tag{S12}$$

where x_{w} is the mole fraction of water and $D_{\mathrm{O_3}}(RH = 0\%)$, $D_{\mathrm{Fe}}(RH = 0\%)$, $H_{\mathrm{O_3}}(RH = 0\%)$, C and D are fitting parameters given in Table S1. Other parameters given in Table S1 are the diffusion coefficient of $\mathrm{O_3}$ in water, $D_{\mathrm{O_3}}^{\circ}$, Henry's law coefficient of $\mathrm{O_3}$ in water, $H_{\mathrm{O_3}}^{\circ}$, and diffusion coefficient of Fe in water, D_{Fe}°. A mixing rule was also derived for comparison following

$$\log H_{\mathrm{O_3}} = wt_{\mathrm{w}} \log H_{\mathrm{O_3}}^{\circ} + (1 - wt_{\mathrm{w}}) \log H_{\mathrm{O_3}}(RH = 0\%), \tag{S13}$$

where wt_{w} is the weight fraction of water in the particles. Equation (S13) was determined without any fitting parameters since $H_{\mathrm{O_3}}^{\circ}$ is taken from previous literature[9,12] and $H_{\mathrm{O_3}}$ at $RH = 0\%$ was derived from KM-SUB. We found that eqn (S11) is a better representation and recommended for use to describe $\mathrm{O_3}$ solubility in XG.

2.2   Reactive uptake coefficient calculated from the KM-SUB model

In addition to deriving aerosol internal composition, KM-SUB also calculated the reactive uptake of $\mathrm{O_3}$, γ, as a function of t and RH is shown in Fig. S9. Initially, $\gamma = 0.5$ due to surface accommodation, then obtaining values on the order of 10^{-4} when absorption equilibrium was established. As reaction continued over minutes to hours when $[\mathrm{O_3}]_{\mathrm{g}}$ rose, γ fell as the concentration of Fe^{2+} dropped near the surface. Unfortunately, gas phase loss of $\mathrm{O_3}$ to aerosol surfaces or uptake coefficients could not be measured with our current setup. We suggest that by measuring changes in gas phase composition and measuring depth resolved aerosol composition with nanometer resolution, would also provide constraints on the other elementary steps in this hetereogeneous reaction system, such as surface accommodation, a postulated surface self-reaction rate constant, a second-order loss process on the surface surface and surface saturation which we were not sensitive to in this study. Together with internal composition derived using STXM/NEXAFS, we speculate that it may be possible to treat all kinetic parameters as free parameters for a global optimization.

2.3 Model sensitivity to diffusion and solubility parameters

The sensitivity of parameters D_{O_3}, D_{Fe} and H_{O_3} to reproduce observed gradients was tested by varying one parameter at a time by a few orders of magnitude with respect to their optimized values in the KM-SUB model while keeping the other two constant. Then, the sum of squared residual values (RSS) was calculated between modelled and observed 2-D profiles. Figure S10 shows the percent difference of RSS from the minimum value, RSS_{fit}. This is presented as $\Delta RSS/RSS_{fit}$ in Fig. S10, where $\Delta RSS = RSS - RSS_{fit}$. When parameters were varied, $\Delta RSS/RSS_{fit}$ increased either symmetrically obtaining a parabolic shape or asymmetrically. When $\Delta RSS/RSS_{fit} = 20\%$, the corresponding range in parameters was typically about 1 order of magnitude or less. The smaller the parameter range to satisfy $\Delta RSS/RSS_{fit} = 20\%$, the more sensitive the fit was to that particular parameter. In Fig. S10i for example, increasing or decreasing H_{O_3} at $RH = 43\%$ caused the RSS to drastically increase, and the parameter range to satisfy $\Delta RSS/RSS_{fit} < 20\%$ was small compared to most others. In Fig. S10h, increasing D_{Fe} by 1 order of magnitude caused a 40% difference in RSS. At $RH = 0\%$, we found more than one local minimum for D_{Fe} as seen in Fig. S10b. However, we are confident that our optimized value represents a global minimum as described later. Notice in Fig. S10n that RSS continually increased when D_{Fe} was decreased, however RSS increased to a plateau at about $\Delta RSS/RSS_{fit} = 5\%$ when D_{Fe} was increased. In general, larger values of D_{Fe} would tend to cause more uniform profiles in α. Figure 3e in the main text shows that profiles were already fairly uniform under these conditions, and increasing D_{Fe} to find a better fit would make little difference in RSS. In other words, our fit was relatively insensitive to increases in D_{Fe} for $RH = 80\%$, although a unique minimum was found, giving confidence in our parameter estimate.

We could not find a unique minimum value for D_{O_3} and H_{O_3} at $RH = 0\%$ due to computational reasons. Decreasing the values of these parameters with respect to their optimized value always resulted in increasing RSS and thus a lower limit where $\Delta RSS/RSS_{fit} = 20\%$ was found. However, we could not perform simulations for D_{O_3} or H_{O_3} at higher than optimized values. The KM-SUB model uses a fixed number of layers and layer spacing defined at the start of the simulation of chemical reaction and molecular diffusion. Accurate predictions were only possible if there are a sufficient number of layers to resolve a gradient in either O_3 or Fe^{2+}. We have found that for higher D_{O_3} or H_{O_3} parameters, gradients in ozone reached greater and greater depths over time. For $RH = 0\%$ only, sensitivity testing

required an unreasonable number of fixed layers and surpassed the computational ability available to us. To resolve this, the total number of layers should dynamically change in time in which layers split for better resolution and merge for less resolution whenever it is needed. Due to most model sensitivity appearing symmetric, we choose a symmetric sensitivity range for D_{O_3} and H_{O_3} at $RH = 0\%$.

We also wished to investigate a global sensitivity when varying more than one parameter simultaneously. Due to limits on computational ability, we could only investigate multi-parameter sensitivity for $RH = 40\%$. First, we randomly sampled D_{O_3} and H_{O_3} thousands of times creating parameter pairs, which were then used to calculate RSS. Then, we used 2-D linear interpolation to generate a gridded RSS surface as a function of D_{O_3} and H_{O_3}. Finally, we applied smoothing using 2-D convolution. The contour plot of the RSS surface in Fig. S11a clearly shows that D_{O_3} and H_{O_3} are highly correlated and in general, a clear minimum cannot be determined. Minimum RSS values appear to fall on a line defined by the product $\log_{10} H_{O_3} \sqrt{D_{O_3}} \simeq -7.7$ indicated in Fig. S11a. This is due to our reactive system being in the regime of reacto-diffusive limitation. A curvature in minimum RSS values deviating from this line is seen for $\log_{10} D_{O_3} < -7$ when the contours applear to gradually align horizontally. This is due to α approaching a homogeneous distribution as a result of D_{O_3} becoming so high. Although it is not entirely clear from the contour plot, minimum RSS values increased slightly from about 1.4×10^3 to 2.8×10^3 when D_{O_3} increased from 10^{-9} to 10^{-2} cm^2 s^{-1} meaning that H_{O_3} should be greater than $\sim 10^{-4}$ mol cm^{-3} atm^{-1}. Considering that $D_{O_3}^{\circ}$ is a physical upper limit of D_{O_3} for $RH < 100\%$, these results are reasonable and line with the finding that O$_3$ solubility is typically greater in organic liquids than in water. Our optimized parameters value are indicated by the black cross and satisfy this condition.

Previously, Berkemeier *et al.*[9] found that D_{O_3} and H_{O_3} were highly correlated and that a unique global minimum in RSS could only be obtained when fixing the bulk reaction rate coefficient. Our bulk reaction rate coefficient (k_{R3}) was fixed, however unique O$_3$ transport and solubility parameters were not found. Although, our fitting algorithm found a global minimum we cannot rule out that another pair of parameters which satisfies $\log_{10} H_{O_3} \sqrt{D_{O_3}} \simeq -7.7$ can fit our data just as well.

We also determined our model sensitivity when all three parameters were allowed to vary simultaneously. RSS contours are shown in Fig. S11b as a function of D_{Fe} and the product $H_{O_3} \sqrt{D_{O_3}}$. The isoline $\log_{10} H_{O_3} \sqrt{D_{O_3}} = -7.7$ is also plotted. We found multiple local minima in this parameter space and a clear global minimum. Our fitted parameters are again plotted as the black cross in Fig. S11b and

appear exactly at the global minimum. From this sensitivity analysis we make two conclusions. The first is that, our observed 2-D profiles of α were a good enough constraint that a unique value of D_{Fe} could be found to minimize the residuals. Second, we found that although $D_{\mathrm{O_3}}$ and $H_{\mathrm{O_3}}$ were coupled, their product $H_{\mathrm{O_3}}\sqrt{D_{\mathrm{O_3}}}$ could be constrained.

2.4 Experimental and model derived parameters in the reacto-diffusive framework

In order to derive an analytical solution for α to compare with our observations, we first define the net flux of O_3 in the gas phase into the condensed phase as

$$J_{\mathrm{net}} = \frac{\gamma\omega}{4}[O_3]_{\mathrm{g}}, \tag{S14}$$

where γ is the reactive uptake coefficient and ω is the mean thermal velocity of O_3. It is important to note that eqn (S14) is the net flux that results in a loss of gas phase O_3 because γ is defined as the probability that a molecular collision on an aerosol particle surface results in an irreversible loss from the gas phase. The first order loss rate of O_3 from the gas phase is then

$$\frac{d[O_3]_{\mathrm{g}}}{dt} = -\frac{\gamma\omega}{4}[O_3]_{\mathrm{g}}N_{\mathrm{p}}S_{\mathrm{p}}, \tag{S15}$$

where N_{p} is the number of particles per volume of air and S_{p} is the surface area of a single particle such that the product $N_{\mathrm{p}}S_{\mathrm{p}}$ is the total surface area of aerosol particles per volume of air. Implicit to eqn (S14) and (S15) is that net O_3 loss in the gas phase equals the Fe^{2+} loss or

$$\frac{d[Fe^{2+}]_{\mathrm{g}}}{dt} = \frac{d[O_3]_{\mathrm{g}}}{dt}, \tag{S16}$$

where $[Fe^{2+}]_{\mathrm{g}}$ is the number of Fe^{2+} atoms in the particle phase per unit volume of air. Typically, $[Fe^{2+}]_{\mathrm{g}}$ is not considered and so a conversion to the more familiar particle phase concentration is as follows,

$$[Fe^{2+}]_{\mathrm{g}} = [Fe^{2+}]N_{\mathrm{p}}V_{\mathrm{p}}, \tag{S17}$$

where $[Fe^{2+}]$ is previously defined as the number of Fe^{2+} atoms in the particle phase per unit volume of particle phase and V_p is the volume of a single particle such that the product $N_p V_p$ is the total volume of aerosol particles per volume of air. Substituting eqn (S16) and (S17) into eqn (S15) yields

$$\frac{d[Fe^{2+}]}{dt} = -\frac{\gamma\omega}{4}[O_3]_g \frac{S_p}{V_p}. \tag{S18}$$

From the 3-D radial profiles derived by the KM-SUB model, O_3 reaction was predicted to have occurred in a thin shell below the surface. Therefore we follow the rate limiting case described in Worsnop $et\ al.$[13] that the uptake of O_3 is controlled by a fast reaction within the reacto-diffusive length much smaller than the particle radius. Following previous studies[13–15],

$$\gamma = \frac{4H_{O_3}RT_p}{\omega}\sqrt{D_{O_3}k_{R3}[Fe^{2+}]}, \tag{S19}$$

where R is the universal gas constant. When substituting in eqn (S19) into (S18), the square-root dependence on the depletion of Fe^{2+} in a particle can be written as

$$\frac{d[Fe^{2+}]}{dt} = -k^D\sqrt{[Fe^{2+}]}, \tag{S20}$$

where

$$k^D = -H_{O_3}[O_3]_g RT_p\sqrt{D_{O_3}k_{R3}}\frac{6}{d_p}, \tag{S21}$$

is the equation for the reacto-diffusive rate constant[1]. We note that S_p/V_p of half spheres on a flat plate is $6/d_p$. Solving eqn (S20) and substituting in eqn (S21) and α from eqn (S1) yields,

$$2\left(\sqrt{\alpha} - \sqrt{\alpha_0}\right) = -H_{O_3}RT_p\sqrt{\frac{D_{O_3}k_{R3}}{[Fe_{tot}]}}\frac{6}{d_p}\int_0^t [O_3]_g\,dt. \tag{S22}$$

Rearranging eqn (S22) and again recognizing that $\phi(t) = \int_0^t [O_3]_g\,dt$ results in the following relationship,

$$\frac{d_p}{3RT_p}\frac{[Fe_{tot}]\left(\sqrt{\alpha} - \sqrt{\alpha_0}\right)}{\phi(t)\sqrt{k_{R3}}} = H_{O_3}\sqrt{D_{O_3}}. \tag{S23}$$

We calculated α from observations for each particle exposed to O_3 to determine the product $H_{O_3}\sqrt{D_{O_3}}$

shown in Fig. S12, where H_{O_3} is the RH dependent Henry's Law coefficient and D_{O_3} is the RH dependent diffusion coefficient for O_3. This product was our only unknown in the reacto-diffusive framework as described in the main text. Values that varied more than 3 times the median absolute deviation are indicated in Fig. S12. The area of each particle was determined from STXM/NEXAFS images to calculate particle circle equivalent diameter, d_p. Approximating all particles as semi-spheres on a flat plate, we calculated their surface to volume ratio, $S_p/V_p = 6/d_p$. The product of the fitted parameters from KM-SUB, is shown as the dotted line in Fig. S12 to compare with observations.

3 Tables

Table S1: Fitting parameters for the Vignes-type equation (eqns (S9)-(S12)). The subscript "x" represents either O_3 or Fe.

	D_x° / cm^2 s^{-1}	$D_x(RH = 0\%)$ / cm^2 s^{-1}	H_x° / mol cm^{-3} atm^{-1}	$H_x(RH = 0\%)$ / mol cm^{-3} atm^{-1}	C	D
D_{O_3}	$1.90 \times 10^{-5\,a}$	7.45×10^{-18}			1.73	-0.17
H_{O_3}			$1.20 \times 10^{-5\,b}$	3.93×10^{-2}	1.21	-0.50
D_{Fe}	$7.19 \times 10^{-6\,c}$	4.53×10^{-18}			0.67	-1.15

[a]Berkemeier $et\ al.$[9], Smith and Kay[12]
[b]Sander[16]
[c]Vanýsek[17]
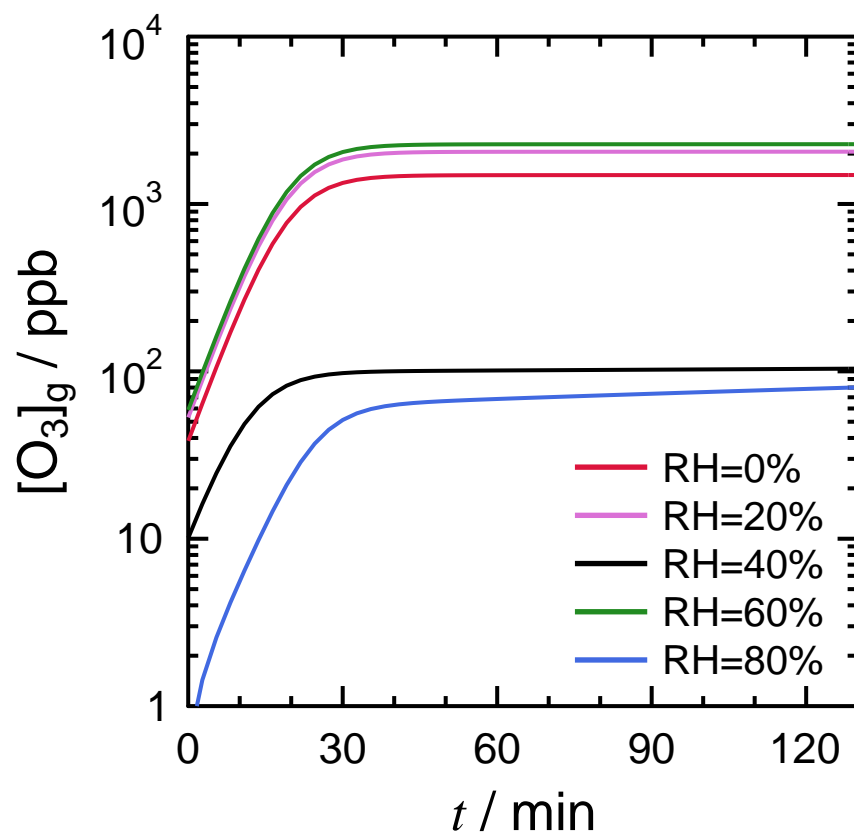
4   Figures

Figure S1:   The observed gas phase ozone concentration, $[O_3]_g$, at standard temperature and pressure as continuous functions in time, t, for all experiments used the KM-SUB model. Relative humidity, RH, for each experiment is indicated.
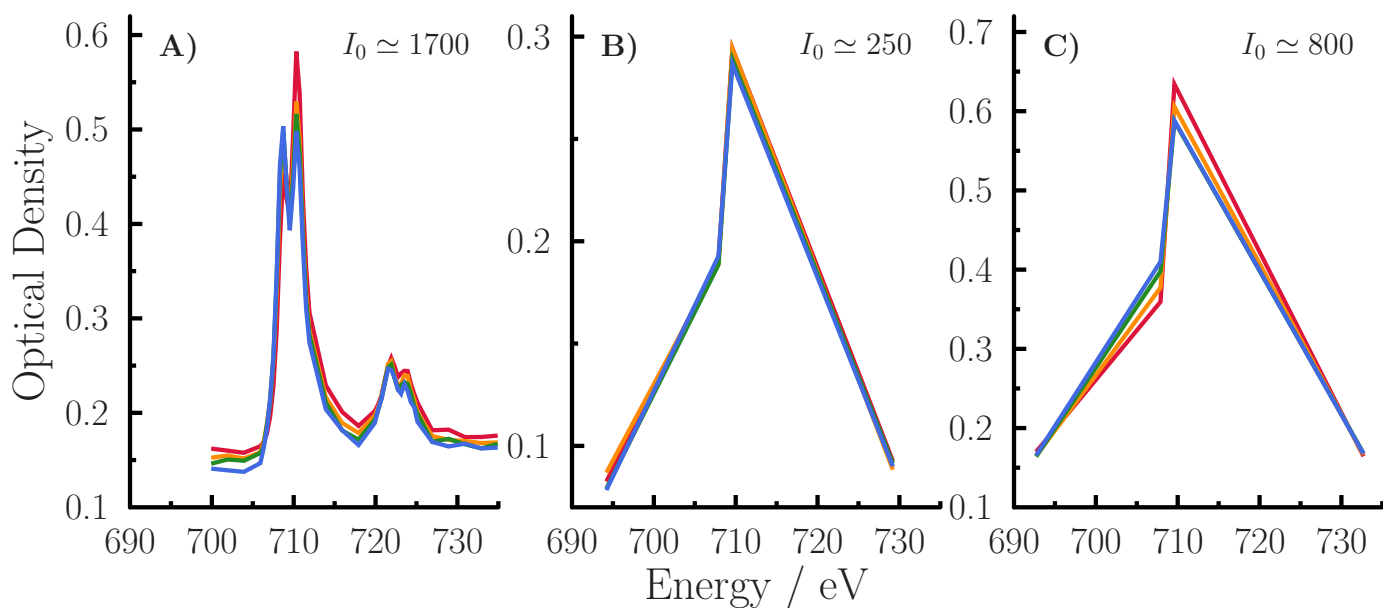
Figure S2: Damage assessment of X-ray exposed particles of xanthan gum (XG) mixed with $FeCl_2$. Blue, green, orange and red colors were acquired one after another and indicate increasing damage. a) A full near edge X-ray absorption fine structure (NEXAFS) spectra over the same particle is shown where each pixel was irradiated with approximately 1700 photons at 50 energy points. b) A map (4 energy points) of particles where each pixel was irradiated with approximately 250 photons. c) A map of particles where each pixel was irradiated with approximately 800 photons.
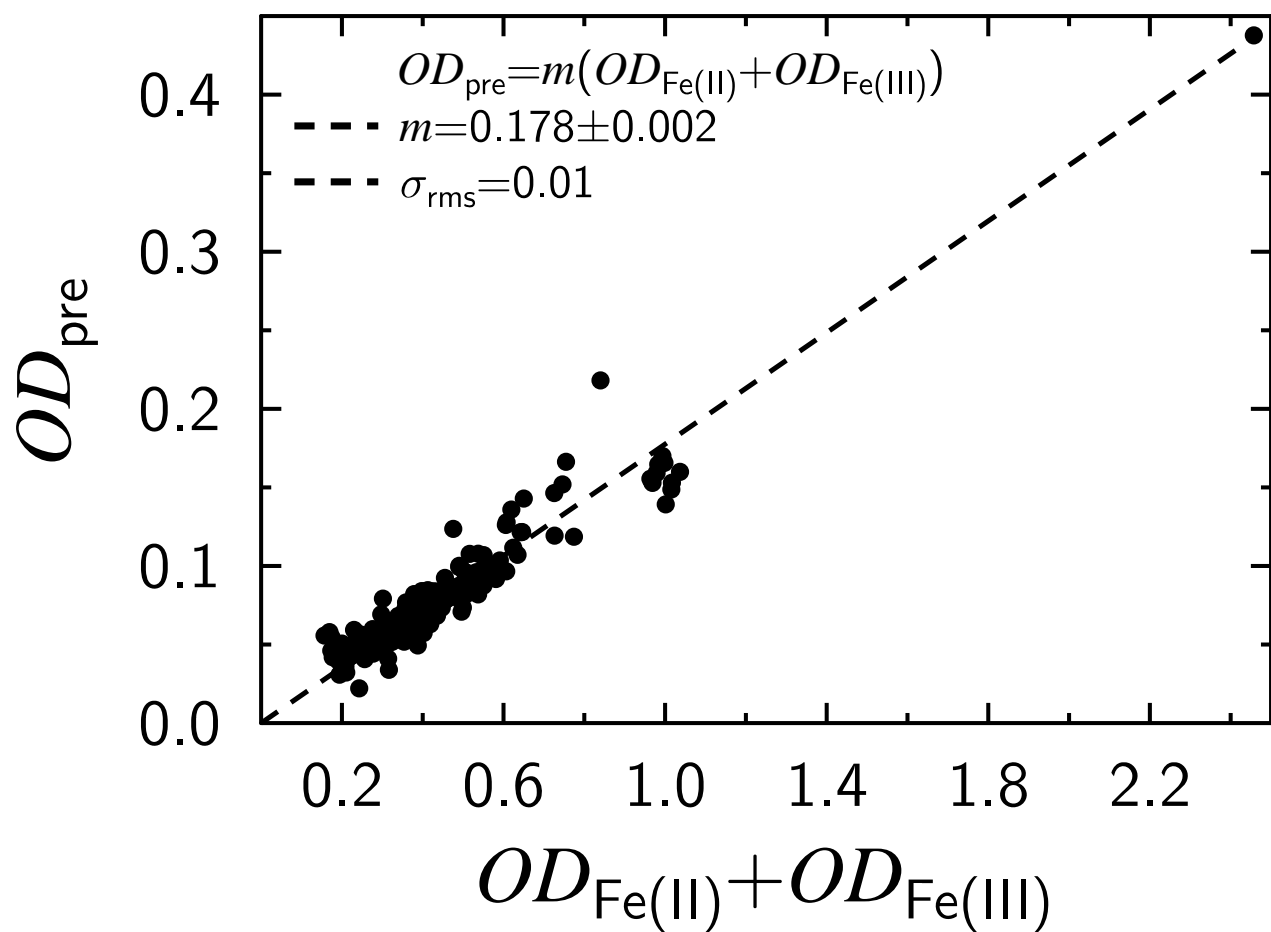
Figure S3: Average optical density derived at the Fe pre-edge, OD_{pre}, as a function of the sum of optical density at the Fe^{2+} and Fe^{3+} peak at 707.8 and 709.5 eV, respectively, or $OD_{Fe^{2+}} + OD_{Fe^{3+}}$. Each symbol is the average over an individual particle. The dashed line is a fit to the linear equation indicated in the figure.
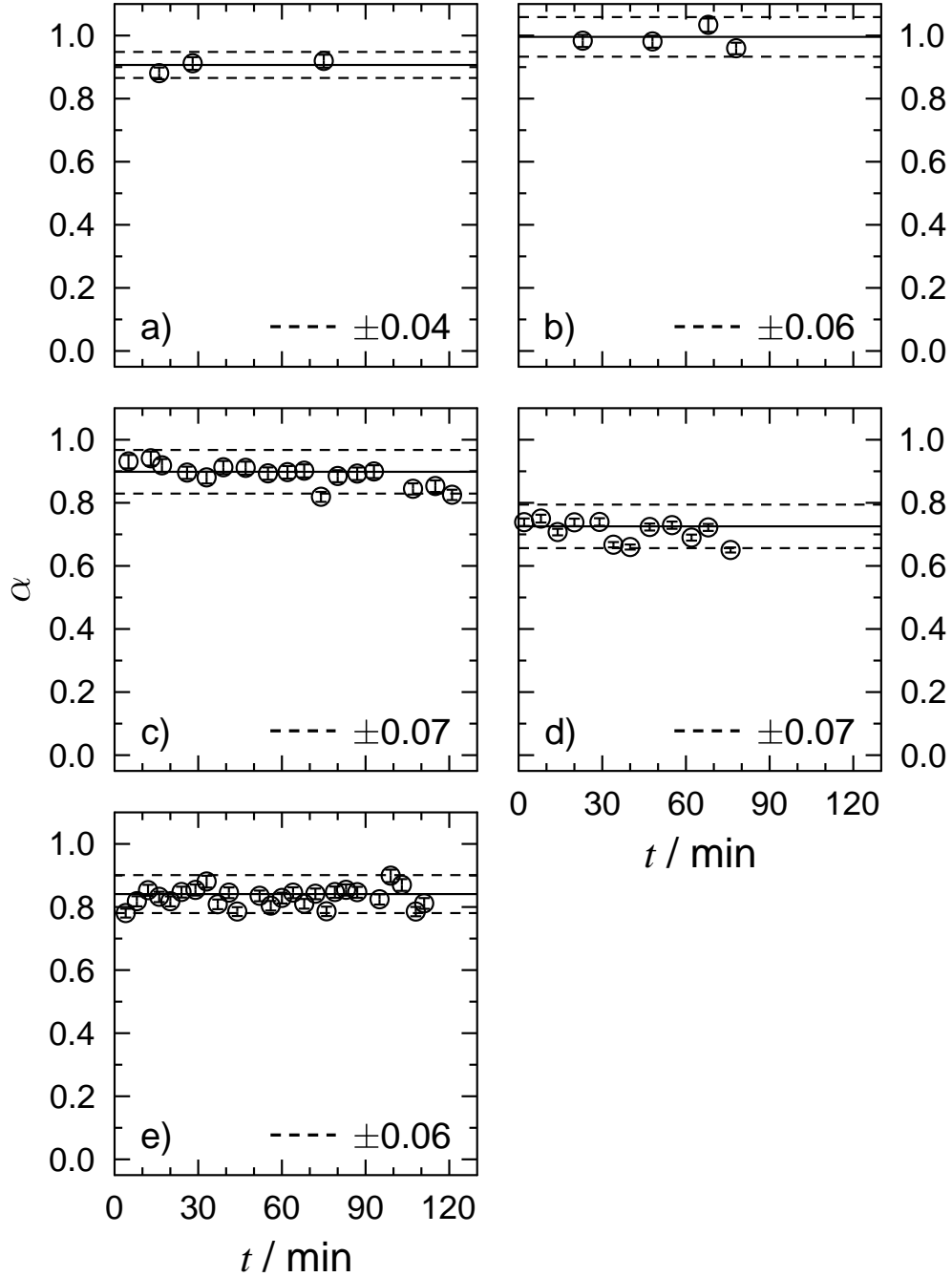
Figure S4: Measured Fe^{2+} fraction, α, as a function of time, t, during oxygen exposure for a) $RH = 0$, b) 22, c) 43, d) 60 and e) 80%. Each data point is determined from approximately 5-25 particles. The error bar indicates the error on the average value propagated from X-ray photon counting statistics. The solid line is the average value of individual particles from Fig. S5. The dotted lines are the standard deviation of α for individual particles shown in Fig. S5.
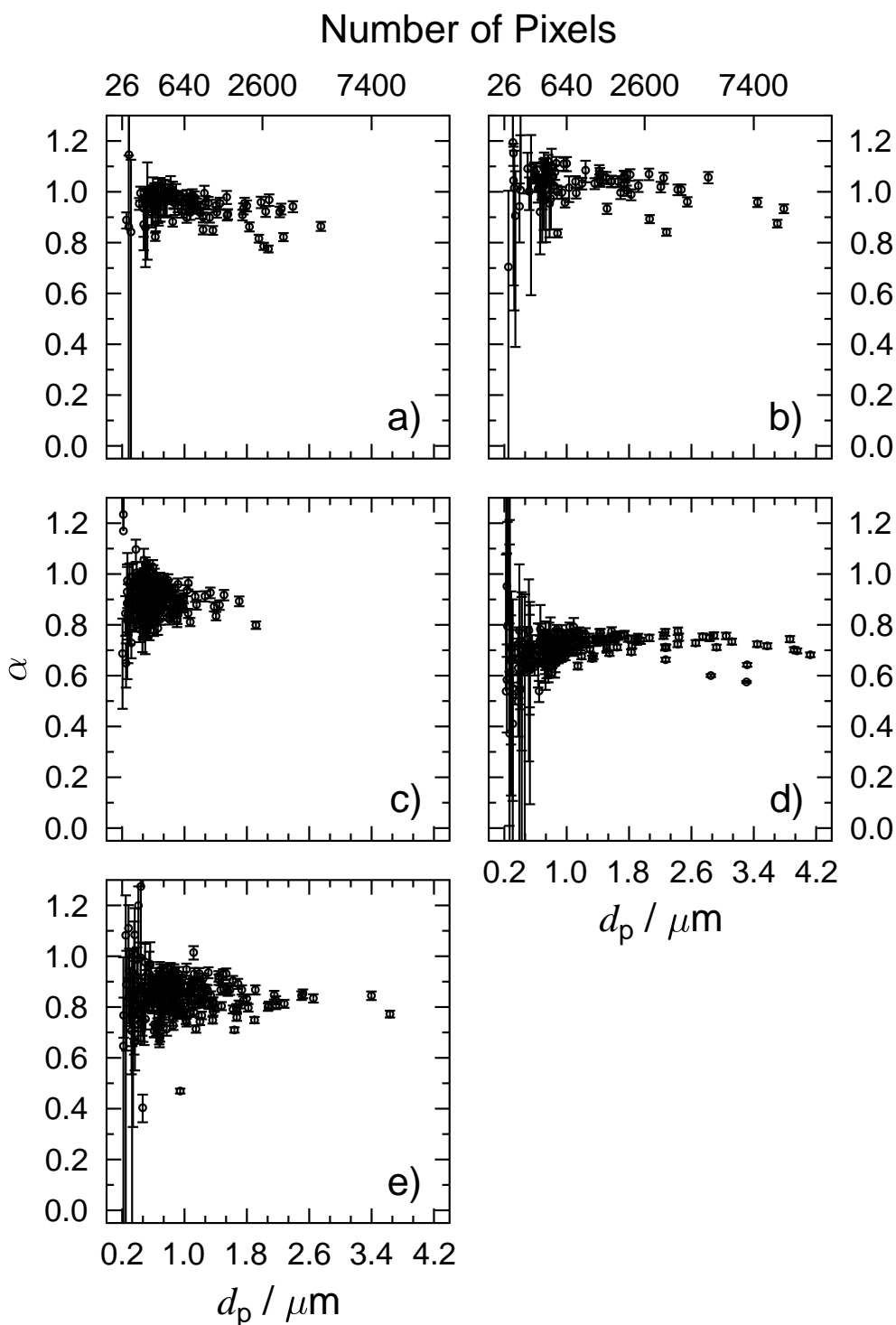
Figure S5: Measured Fe^{2+} fraction, α, as a function of particle diameter, d_p, during O_2 exposure for a) $RH = 0$, b) 22, c) 43, d) 60 and e) 80%. Each data point is an average over a single particle where the number of pixels per particle is given in the top abscissa. The data here was also used to determine averages in Fig. S4. Error bars indicate the error on the average value propagated from X-ray photon counting statistics. The standard deviation of α for individual particles is not shown here, but included in Fig. S4.
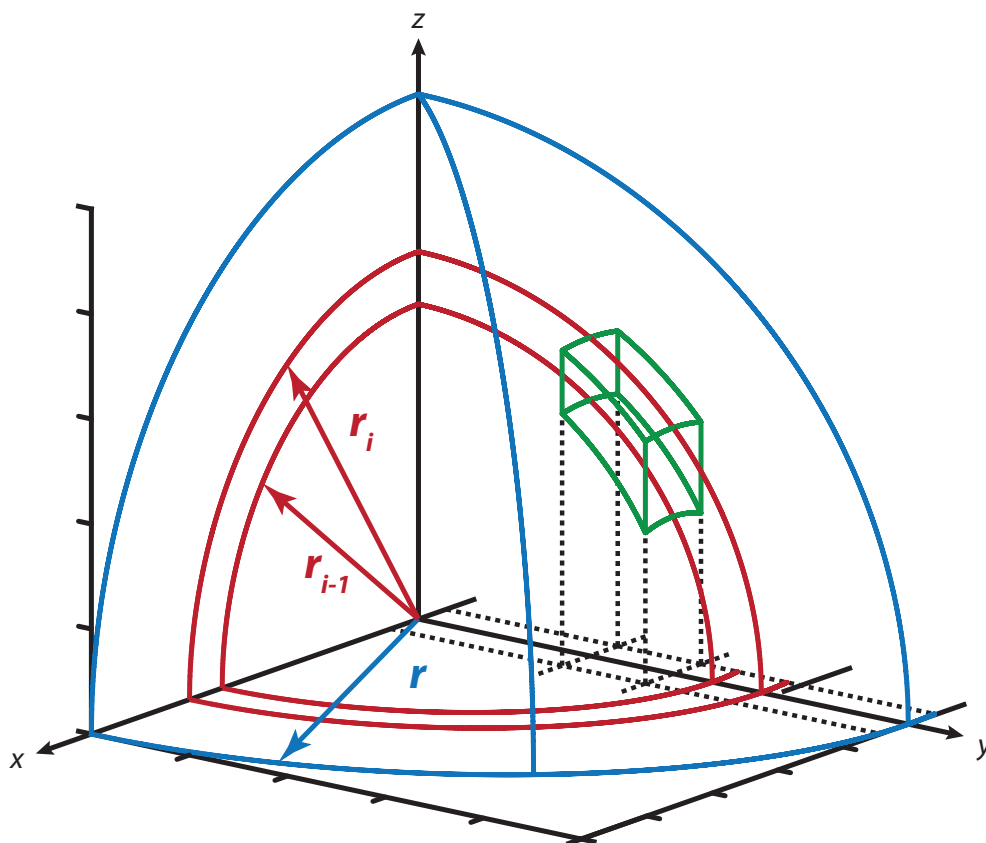
Figure S6: Geometric representation of a 2-D projection on a grid box of a finite volume from a spherical shell outlined in green inside of an spherical aerosol particle. The particle radius is r and outlined in blue. The shell outside and inside diameter is r_i and r_{i-1}, respectively, and outlined in red. Black solid lines are the axis and black dashed lines indicate the grid box.
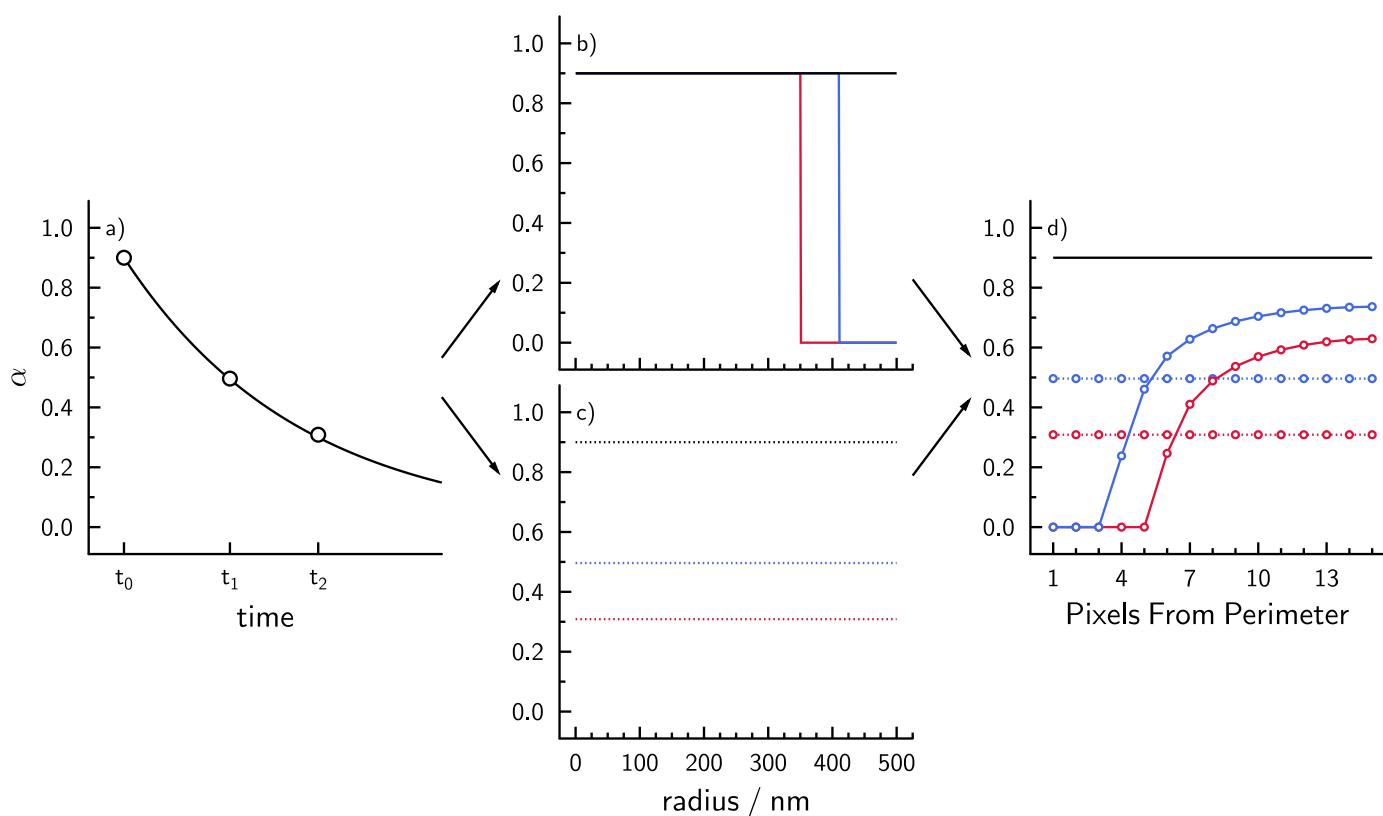
Figure S7: Examples of uniform and inhomogeneous 3-D radial and 2-D column integrated profiles of Fe^{2+} fraction, α. A hypothetical decay of α over time is shown in a) where t_0 is the initial value and t_1 and t_2 are at later arbitrary times. The symbols and line represent possible measurements and model predictions of α averaged over all particles. Radial particle profiles of α in 3-D are shown which are b) completely inhomogeneous and c) uniform, where black, blue and red color correspond to t_0, t_1 and t_2. When averaged over the entire particle, α in both b) and c) are equivalent and shown in a). Column integrated profiles are shown in d) where solid and dotted lines are from calculated from b) and c) respectively.
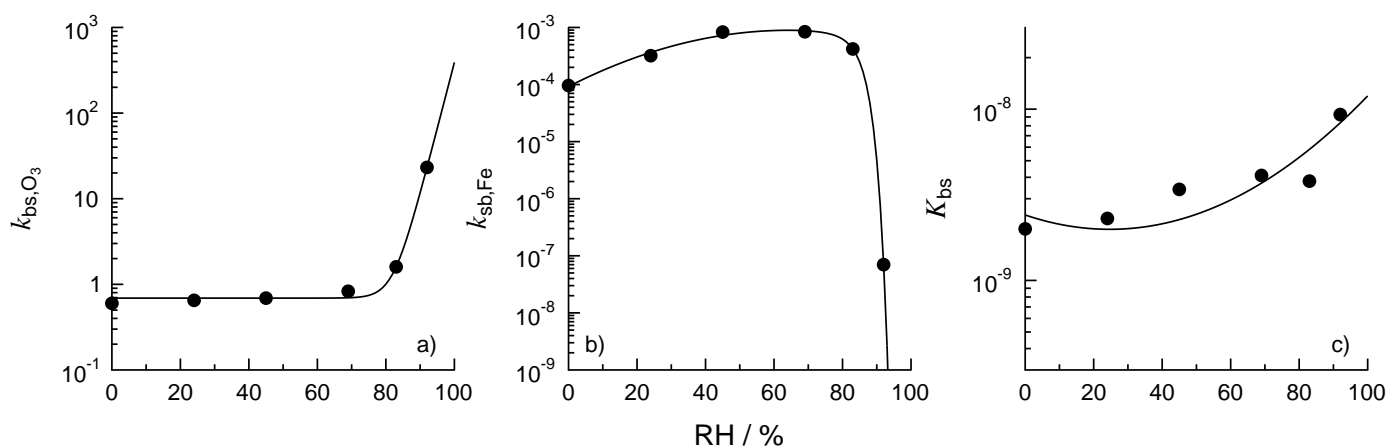
Figure S8: Relative humidity, RH, dependent parameters used in the KM-SUB model. These parameters are the bulk to surface transfer rate coefficient for O_3, k_{bs,O_3}, the surface to bulk transfer rate coefficient, k_{sb}, and the surface equilibrium constant, K_{bs}. Symbols are taken from Berkemeier et al.[9] and solid lines are parameterizations as a function of RH.
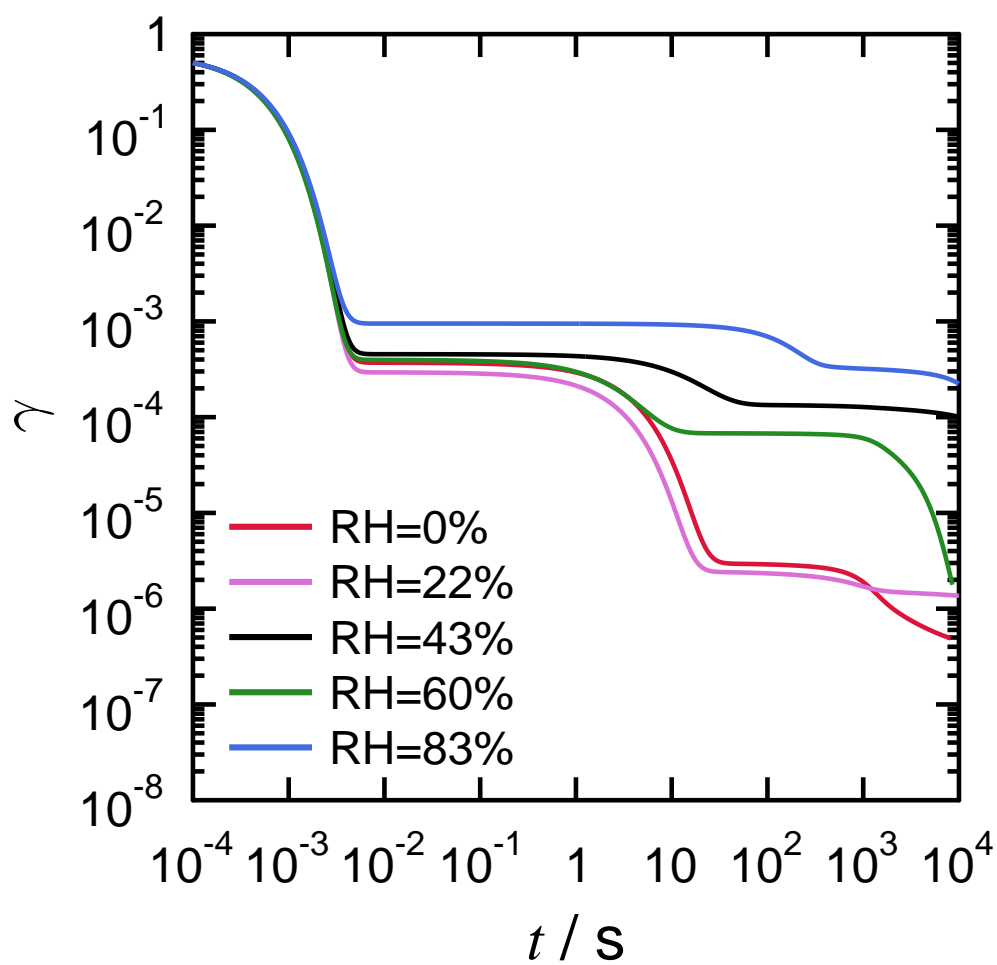
Figure S9: Calculated reactive uptake coefficients, γ, from the KM-SUB model as a function of time, t, for all experiments. Relative humidity, RH, is indicated.
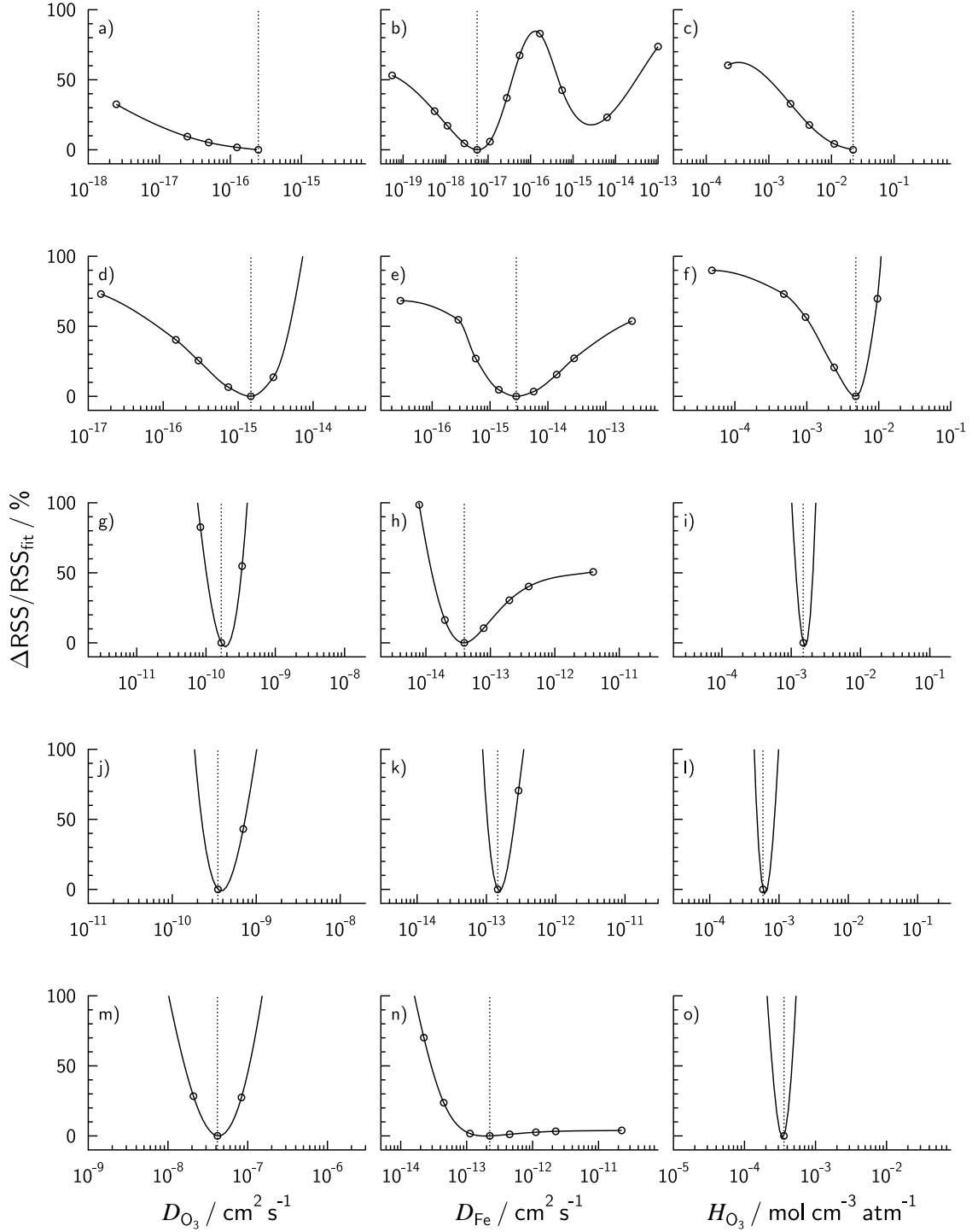
Figure S10: Model sensitivity on the fitted ozone diffusion coefficient, D_{O_3}, iron diffusion coefficient, D_{Fe}, and ozone Henry's Law constant, H_{O_3}, at (a-c) 0%, (d-f) 22%, (g-i) 43%, (j-l) 60% and (m-o) 80%. The percent change in the sum of the squared residual values (RSS) was determined as $\Delta RSS/RSS_{fit}$, where RSS_{fit} is the minimized value and ΔRSS is the deviation from RSS_{fit} when a parameter is raised or lowered from its optimal value indicated by the vertical dotted line. Symbols are individually calculated points spanning 4 orders of magnitude and solid lines are a third order spline interpolation.
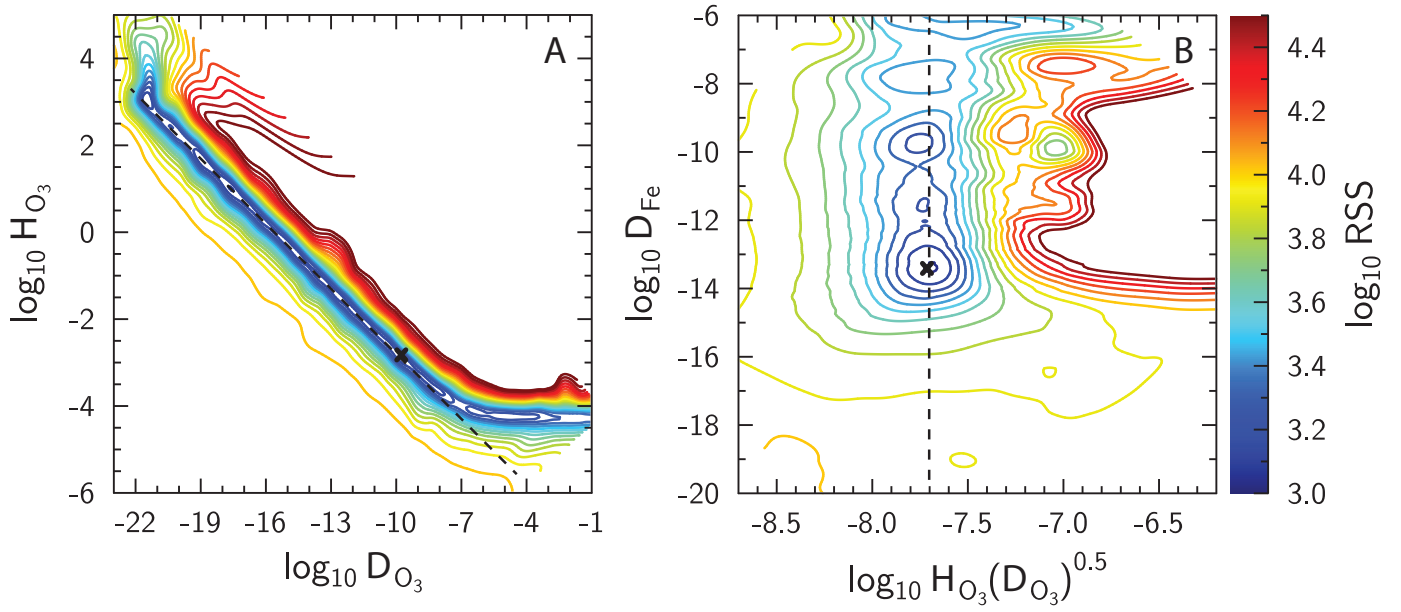
Figure S11: Model sensitivity on the fitted parameters in the KM-SUB model. (a) The ozone diffusion coefficient, D_{O_3}, and Henry's Law constant, H_{O_3}, was varied simultaneous keeping the iron diffusion coefficient, D_{Fe}, constant. (b) All three parameters were varied simultaneously where the abscissa is the product of $H_{O_3}\sqrt{D_{O_3}}$. The dashed line indicates $H_{O_3}\sqrt{D_{O_3}} = -7.7$ The color contours is the sum of the squared residual values (RSS) on a logarithmic scale.
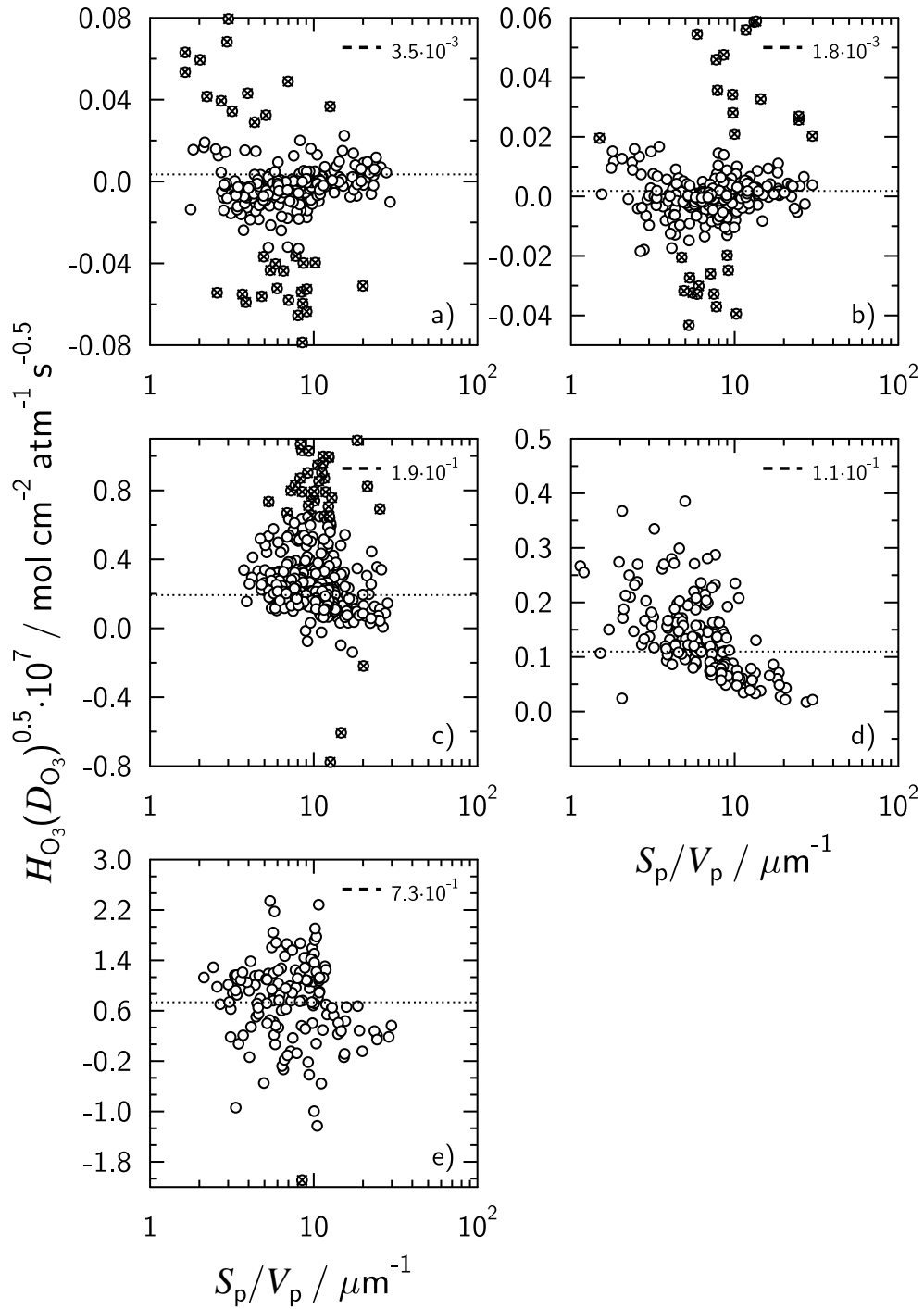
Figure S12: The product of Henry's Law coefficient for ozone, H_{O_3}, and the square root of the diffusion coefficient of ozone, D_{O_3}, or $H_{O_3}\sqrt{D_{O_3}}$, as a function of particle surface to volume ratio, S_p/V_p, at a relative humidity RH of a) 0%, b) 22%, c) 43%, d) 60% and e) 80%. Each data point is an individual particle. Values which deviate more than 3x the average deviation of the median are indicated with an "x". The dotted line is derived from fitted parameters and its value indicated in each panel.

References

[1] S. S. Steimer, M. Lampimäki, E. Coz, G. Grzinic and M. Ammann, *Atmos. Chem. Phys.*, 2014, **14**, 10761–10772.

[2] C.-E. Brunchi, M. Bercea, S. Morariu and M. Dascalu, *Journal of Polymer Research*, 2016, **23**, 123.

[3] T. Huthwelker, V. Zelenay, M. Birrer, A. Krepelova, J. Raabe, G. Tzvetkov, M. G. C. Vernooij and M. Ammann, *Rev. Sci. Instrum.*, 2010, **81**, 113706.

[4] J.-D. Förster, C. Pöhlker, C. Gurk, M. Lamneck, M. Ammann, U. Pöschl and M. O. Andreae, *Atmos. Mech. Tech.*, 2019, to be submitted.

[5] R. C. Moffet, T. Henn, A. Laskin and M. K. Gilles, *Anal. Chem.*, 2010, **82**, 7906–7914.

[6] R. C. Moffet, A. V. Tivanski and M. K. Gilles, in *Fundamentals and Applications in Aerosol Spectroscopy*, ed. R. Signorell and J. P. Reid, Taylor and Francis Group, LLC, Boca Raton, FL, 2011, ch. 17. Scanning Transmission X-ray Microscopy: Applications in Atmospheric Aerosol Research, pp. 419–462.

[7] L. A. J. Garvie, A. J. Craven and R. Brydson, *Am. Mineral.*, 1994, **79**, 411–425.

[8] R. C. Moffet, H. Furutani, T. C. Rödel, T. R. Henn, P. O. Sprau, A. Laskin, M. Uematsu and M. K. Gilles, *J. Geophys. Res.*, 2012, **117**, D07204.

[9] T. Berkemeier, S. S. Steimer, U. K. Krieger, T. Peter, U. Pöschl, M. Ammann and M. Shiraiwa, *Phys. Chem. Chem. Phys.*, 2016, **18**, 12662–12674.

[10] R. D. Shannon, *Acta Cryst.*, 1976, **32**, 751–767.

[11] K. W. Dawson, M. D. Petters, N. Meskhidze, S. S. Petters and S. M. Kreidenweis, *J. Geophys. Res.*, 2016, **121**, 11803–11818.

[12] R. S. Smith and B. D. Kay, *Nature*, 1999, **398**, 788–791.

[13] D. R. Worsnop, J. W. Morris, Q. Shi, P. Davidovits and C. E. Kolb, *Geophys. Res. Lett.*, 2002, **29**, GL015542.

[14] D. R. Hanson, A. R. Ravishankara and S. Solomon, *J. Geophys. Res.*, 1994, **99**, 3615–3629.

[15] D. R. Hanson and E. R. Lovejoy, *Science*, 1995, **267**, 1326–1328.

[16] R. Sander, *Atmos. Chem. Phys.*, 2015, **15**, 4399–4981.

[17] P. Vanýsek, in *CRC Handbook of Chemistry and Physics, 82nd edition*, ed. D. R. Lide, CRC Press, Boca Raton, Fl, USA, 2001, ch. Ionic conductivity and diffusion at infinite dilution, pp. 5–95.